



AIAA 98-2435

A Refined Method for DNS of Transition in
Interacting Boundary Layers

U. Maucher, U. Rist and S. Wagner

Universität Stuttgart

Stuttgart, Germany

29th AIAA Fluid Dynamics Conference
June 15-18, 1998 / Albuquerque, NM

A REFINED METHOD FOR DNS OF TRANSITION IN INTERACTING BOUNDARY LAYERS

U. Maucher*, U. Rist†, S. Wagner‡

Institut für Aerodynamik und Gasdynamik, Universität Stuttgart
Stuttgart, Germany

Abstract

In direct numerical simulations (DNS) of the transition in laminar separation bubbles the definition of a well-posed free-stream boundary condition is crucial. Different, partially contradicting properties are required: first of all, separation is forced by prescribing the streamwise velocity component. The boundary layer thickness grows rapidly and accordingly disturbance waves extend far out into the potential flow causing oscillations at the free-stream boundary. Displacement effects of the separation bubble influence the surrounding potential flow by the so-called viscous-inviscid boundary-layer interaction. To fulfill the requirements, either the integration domain has to be sufficiently high or a state-of-the-art boundary layer interaction model based on the theory of thin airfoils can be applied. If the Reynolds number is increased, neither of both possibilities is applicable and DNS results become strongly affected by the height of the integration domain. Therefore, an improved model for larger Reynolds numbers has been developed which meets the above mentioned requirements. The method is validated by variations of the height of the integration domain and by comparisons with experiments. It is shown, that even if the height of the integration domain covers only one boundary-layer thickness, the model works properly.

1 Introduction

A boundary layer subject to a strong adverse pressure gradient is susceptible to separation. In the separated region, disturbance waves, so-called Tollmien-Schlichting (TS-) waves, are strongly amplified and transition to turbulence takes place.

The increased dissipation causes momentum transfer towards the wall and finally forces the boundary layer to re-attach. Besides this more general understanding, the physics of laminar separation bubbles (LSB) is still not well understood. Besides the acceleration of transition and the according higher skin friction, laminar separation bubbles have strong impact on the aerodynamic properties of airfoils through the interaction of the boundary layer and the surrounding potential flow, the viscous-inviscid interaction. Displacement effects of the boundary layer can change the potential flow in the separated region or even worse, around the entire airfoil. A typical pressure plateau is generated near the separated region followed by a sudden pressure increase at the end of the bubble.

As the computers became more powerful, DNS turned out to be a well suited tool to investigate the physics of laminar separation bubbles. On the one hand, DNS can achieve very low (numerical) turbulence to investigate the self-excited behavior of separation bubbles (Gruber [3, 2], Lin & Pauley [5]). On the other hand, the interaction of special 2D and 3D disturbances is investigated in controlled numerical “experiments” (Gruber 2D). Rist [7] and Rist *et al.* [9, 10] were the first to perform controlled simulations of the transition in a laminar separation bubble. By decelerating a Blasius boundary layer to $\approx 91\%$ of the initial velocity Rist *et al.* forced the boundary layer to separate and a separation bubble to form, where the Reynolds number with the displacement thickness at the separation location was about $Re_{\delta_{1,s}} = 1250$. Rist *et al.* obtained a strictly convective behavior of all disturbance waves in the investigated test cases. If the Reynolds number was further increased to $Re_{\delta_{1,s}} = 2400$ Maucher *et al.* [6] found temporal growth of 3D modes, with the presence of a saturated 2D TS-wave (amplitude $\approx 20\%U_\infty$) in the re-attachment region. This growth increases if the separation bubble is bigger. However, comparisons with experiments proved to become more difficult at larger Reynolds numbers. Since DNS aim at the examination of mechanisms which are likely

*Research Assistant.

†Senior Research Scientist.

‡Professor, Member AIAA.

to be present or already identified in experimental or free-flight conditions it is crucial to reproduce these conditions in DNS as good as possible. In that way the relevance of the numerical findings for real flows is guaranteed.

Therefore, since the seventies strong attempts to model the boundary-layer interaction in numerical schemes were made. Now, “viscous-inviscid boundary-layer interaction models” are frequently used for boundary layer calculations in flat integration domains, where the wall-normal extension is very small compared with the streamwise extension. In such models the initially prescribed (inviscid) potential velocity distribution u_p is superposed with a viscous component (index v) due to the displacement of the boundary layer. The displacement is regarded as a modification of the shape of the wall contour and is modeled with a distribution of sources and sinks at the wall. The velocity distribution u_p is updated by adding the streamwise velocity component u_v which is induced by the sources at the wall. Employing the theory of thin airfoils [11], the sources can be easily calculated (Veldman [12]):

$$v_v(x) = \frac{d}{dx}(u_p \delta_1), \quad q(x) = \frac{1}{2}v_v(x), \quad (1)$$

where δ_1 denotes the displacement thickness.

Gruber [2] applied such a model to his DNS code for the investigation of 2D instability in laminar separation bubbles. He shows that the viscous component v_v represents a relation between the wall-normal velocity at the free-stream boundary $v(x, y = y_e)$ and an inviscid part:

$$v_v(x) = v(x, y_e) - \int_0^{y_e} \frac{\partial v_p}{\partial y} dy = v(x, y_e) + y_e \frac{du_p}{dx}. \quad (2)$$

For small separation bubbles he obtained reliable results (Reynolds number $Re_{\delta_{1,s}} \approx 600$).

Tests with such models at Reynolds numbers typical for mid-chord bubbles of glider wing-sections or high-lift devices ($Re_{\delta_{1,s}} \approx 2500$) failed. At best, only coarse qualitative agreement with the experiment can be obtained. Such simulations demand a tall integration domain and the theory of thin airfoils increasingly overestimates the streamwise viscous component u_v in higher integration domains. Moreover, disturbance waves extend far out into the potential flow and cause oscillations at the upper boundary which, in consequence, are modeled as source distribution at the wall. Errors due to the simplifications in the model (i.e., the displacement is modeled at the wall and not in the boundary layer, where it originates) decay

only slowly in streamwise direction ($\propto 1/x$) compared to TS-waves, which might be generated far upstream of the bubble by such errors. If once generated, they are amplified exponentially to such amplitudes which can exceed the amplitude of the initiating errors in the separated region by far, rendering the DNS useless.

However, in DNS of LSB at high Reynolds numbers there are numerical motivations for the application of an interaction model. Imposing the velocity distribution in a low domain has a very rigid impact on the velocity distribution at the edge of the boundary layer. Displacement effects are mostly suppressed. Very high domains allow for changes of the potential flow in wall-normal direction. The velocity at the edge of the boundary layer thus differs from the prescribed potential velocity distribution at the upper boundary of the integration domain. If the height of the integration domain is varied, the edge-velocity distribution therefore changes in spite of similar boundary conditions. A well-defined interaction model has to capture the displacement effects properly, simultaneously avoiding the dependency on the height of the domain.

2 Numerical Method

2.1 Governing equations

The DNS numerical scheme is based on the complete incompressible Navier-Stokes equations in vorticity-transport formulation [8, 4]

$$\begin{aligned} \frac{\partial \omega_x}{\partial t} + \frac{\partial}{\partial y}(v\omega_x - u\omega_y) + \frac{\partial}{\partial z}(w\omega_x - u\omega_z) &= \tilde{\Delta} \omega_x, \\ \frac{\partial \omega_y}{\partial t} + \frac{\partial}{\partial x}(u\omega_y - v\omega_x) + \frac{\partial}{\partial z}(w\omega_y - v\omega_z) &= \tilde{\Delta} \omega_y, \\ \frac{\partial \omega_z}{\partial t} + \frac{\partial}{\partial x}(u\omega_z - w\omega_x) + \frac{\partial}{\partial y}(v\omega_z - w\omega_y) &= \tilde{\Delta} \omega_z, \end{aligned}$$

$$\text{with} \quad \tilde{\Delta} = \frac{1}{Re} \frac{\partial^2}{\partial x^2} + \frac{\partial^2}{\partial y^2} + \frac{1}{Re} \frac{\partial^2}{\partial z^2} \quad (3)$$

which are solved in a rectangular integration domain (figure 1). ω denotes the vorticity. u, v, w are the velocity components in streamwise (x), wall-normal (y), and spanwise (z) direction. All variables are non-dimensionalized by a reference length \hat{L} , by the velocity \hat{U}_∞ , and the Reynolds number $Re = \hat{U}_\infty \hat{L} / \hat{\nu}$, where $\hat{\cdot}$ denotes dimensional variables and $\hat{\nu}$ is the kinematic viscosity:

$$\begin{aligned} x &= \frac{\hat{x}}{\hat{L}}, \quad y = \sqrt{Re} \frac{\hat{y}}{\hat{L}}, \quad z = \frac{\hat{z}}{\hat{L}}, \\ u &= \frac{\hat{u}}{\hat{U}_\infty}, \quad v = \sqrt{Re} \frac{\hat{v}}{\hat{U}_\infty}, \quad w = \frac{\hat{w}}{\hat{U}_\infty}. \end{aligned} \quad (4)$$

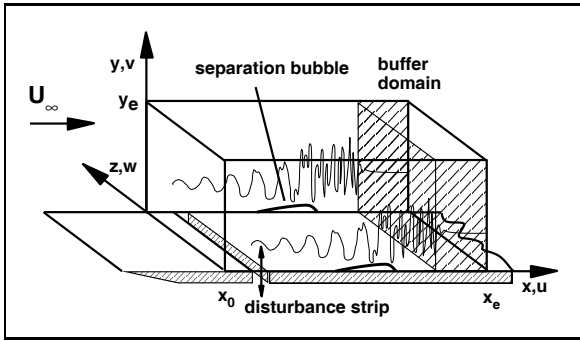


Figure 1: Integration Domain.

This leads to the definition of the non-dimensionalized vorticity components:

$$\begin{aligned}\omega_x &= \frac{1}{Re} \frac{\partial v}{\partial z} - \frac{\partial w}{\partial y}, \\ \omega_y &= -\frac{\partial u}{\partial z} + \frac{\partial w}{\partial x}, \\ \omega_z &= \frac{\partial u}{\partial y} - \frac{1}{Re} \frac{\partial v}{\partial x}.\end{aligned}\quad (5)$$

The velocity components can be derived from three Poisson equations:

$$\frac{\partial^2 u}{\partial x^2} + \frac{\partial^2 u}{\partial z^2} = -\frac{\partial \omega_y}{\partial z} - \frac{\partial^2 v}{\partial x \partial y}, \quad (6)$$

$$\tilde{\Delta} v = \frac{\partial \omega_x}{\partial z} - \frac{\partial \omega_z}{\partial x}, \quad (7)$$

$$\frac{\partial^2 w}{\partial x^2} + \frac{\partial^2 w}{\partial z^2} = \frac{\partial \omega_y}{\partial x} - \frac{\partial^2 v}{\partial y \partial z}. \quad (8)$$

2.2 Boundary conditions and discretization

In *spanwise direction* a spectral ansatz is applied which implies periodic boundary conditions. The equations are solved with a highly efficient, parallelized finite difference method, 4th order accurate in time (Runge-Kutta) and space. Due to the spectral ansatz in spanwise direction the u and w Poisson-equations (6, 8) can be solved independently for each spanwise spectral mode. They reduce to ODEs in streamwise direction and lead to penta-diagonal systems. Only the v -equation (7) has to be solved iteratively by a line relaxation method accelerated by a multigrid algorithm. The spectral ansatz allows to specify different boundary conditions for the 2D and 3D part of the flow.

Since the *free-stream boundary* is in the potential flow, all vorticity components vanish and are set to zero. The inviscid streamwise velocity component u_p is prescribed for the 2D part. With the

continuity-equation

$$\frac{\partial v}{\partial y} = -\frac{\partial u}{\partial x} \quad (9)$$

a 2D von-Neumann condition for v is defined. It allows for a wall-normal velocity component due to displacement effects even if no interaction model is applied. For the 3D part, exponential decay of the wall-normal velocity is assumed

$$\frac{\partial v_{3D}}{\partial y} = -\frac{\alpha_k^*}{\sqrt{Re}} v_{3D}, \quad (10)$$

where $\alpha_k^* = \sqrt{\alpha_e^2 + (\gamma_k)^2}$ denotes a special wavenumber for each spectral mode k which consists of the respective spanwise wavenumber γ_k and a streamwise wave-number α_e which is considered to be representative for the whole streamwise extent of the integration domain (Fasel *et al.* [1]). In the potential flow, this condition derives the exact solution for linear TS-waves with the streamwise wave number α_e . In the progress of a rapid breakdown into fine length scales downstream of the separation bubble, small vortices are injected into the previously undisturbed potential flow. A buffer domain at the free-stream boundary damps the wall-normal derivatives of the vorticity-transport equations to zero when the vortices approach the boundary and finally their wall-normal propagation is stopped. The assumption of inviscid flow at the very boundary remains valid.

At the *inflow boundary*, steady Falkner-Skan profiles, usually Blasius profiles are prescribed. The 3D part of the flow is set to zero. Disturbances are forced by wall-normal suction and blowing in a disturbance strip at the *wall*. Except in the disturbance strip, the no-slip condition is applied at the *wall*.

The unsteady vorticity components are smoothly damped to steady-state values in a buffer domain upstream of the *outflow boundary* [4]. Consequently, the unsteady velocity components also decay exponentially in streamwise direction and vanish at the outflow.

2.3 Boundary-layer interaction-model

To meet the requirements on the interaction model in simulations of separation bubbles at higher Reynolds numbers, the inviscid theory has to be applied without such assumptions as they are made in the theory of thin airfoils. The viscous component $\vec{v}_{v,i}$ is modeled at each Δn -th of the total of N streamwise grid points in the limits

from n_1 near the inflow boundary to n_2 upstream of the buffer domain at the outflow boundary, resulting in $I = 1 + (n_2 - n_1)/\Delta n$ discrete sources \vec{q}_j : $\vec{v}_{v,i} = C_v \vec{q}_j$. The indices i and j denote the streamwise positions of the viscous velocity component $v_v(x_i)$ and of the source $q(x_j)$, respectively, where $1 \leq i, j \leq I$. The matrix C_v with constant coefficients $c_{v,ij} = \frac{1}{2\pi} \frac{y_e}{\xi_{ij}^2 + y_e^2}$, in which ξ_{ij} denotes the streamwise distance from the source ($x_i - x_j$), is inverted once at the beginning of the DNS. Since the matrix C_v is ill conditioned especially in high integration domains and for narrow spacing of the sources, a minimum spacing considerably larger than the streamwise discretization is required ($\Delta n > 1$), limiting the total number I of sources used. Finally, the streamwise viscous velocity component is calculated from $\vec{u}_{v,n} = C_u \vec{q}_j$, where the $(n_2 - n_1 + 1) \times I$ matrix C_u has the constant coefficients $c_{u,nj} = \frac{1}{2\pi} \frac{\xi_{nj}}{\xi_{nj}^2 + y_e^2}$.

The boundary-layer interaction model is implemented into the multigrid scheme of the v -Poisson equation for the 2D part. The boundary conditions of the 3D part are not effected. During the single multigrid cycles of the 2D part, the von-Neumann condition at the free-stream boundary is fixed. At the end of the cycle the viscous part v_v (eqn. 2) is calculated to update the viscous streamwise component to finally get a new von-Neumann condition for the v -Poisson equation $\frac{\partial v}{\partial y} = -\frac{d(u_v + u_p)}{dx}$. It turned out that u_v should be adapted with an under-relaxation of 0.55 for optimum convergence. This procedure is repeated for the first three of a total of eight multigrid-cycles, on the one hand, since the variation of u_v stops decaying from one cycle to the next. On the other hand, the convergence of the multigrid scheme is much worse when the model is active than without it.

In order to suppress a strong upstream influence of the interaction model, the mean $\bar{u}_v(x)$ and the Fourier-amplitude U_v of $u_v(x, t)$ are computed and checked in each TS-period (figure 2a). Upstream of a position $x_{ia}(t)$, where the amplitude $U_v(x)$ exceeds a limit of $\epsilon_{ia} = 2 \times 10^{-4}$ (figure 2b), $u_v(x, t)$ is described by a polynomial function f_c which is continuous up to its first derivative (figure 2c) and approximates the mean $\bar{u}_v(x)$ in the past period. Downstream of x_{ia} the polynomial and the instantaneous values are weighted by $[1 - c_i(x)] f_c(x, t) + c_i(x) u_v(x, t)$ to guarantee a smooth change to the domain further downstream where instantaneous u_v values are applied (figure 2d). Sudden changes of $x_{ia}(t)$ at the step from one TS-period to the next are avoided by a smooth temporal adaption of $c_i(x)$.

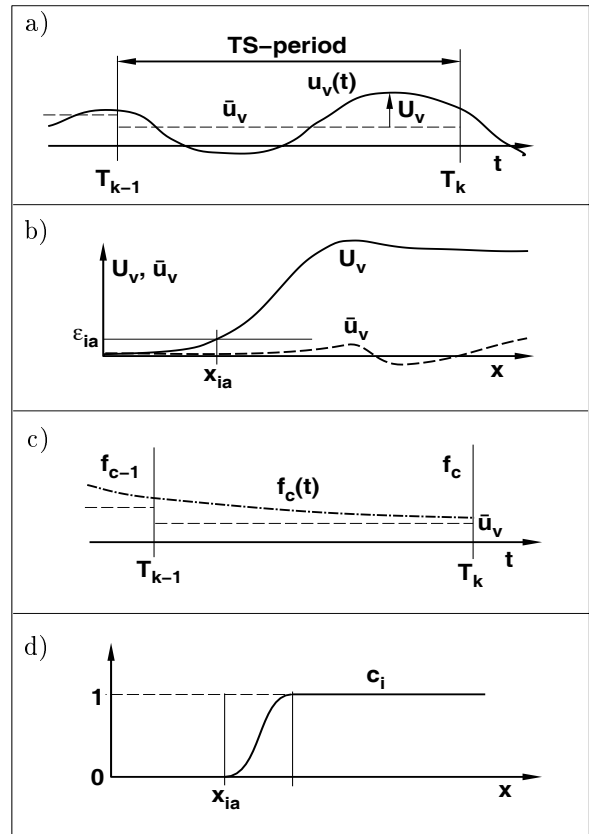


Figure 2: Interaction model: a) sketch of instantaneous induced streamwise velocity u_v , its mean \bar{u}_v (dashed) and amplitude U_v (arrow) in TS-Period (T_{k-1}, T_k), b) qualitative streamwise distribution of the mean \bar{u}_v and amplitude U_v of the induced velocity in a TS-period, c) polynomial $f_c(t)$ if $U_v(x)$ is low, d) streamwise distribution of the blending function used for the change from the polynomial to instantaneous values.

Nevertheless, even very close to the inflow boundary the model originally predicted comparably strong oscillations. The buffer domain at the upper boundary proved necessary to keep these oscillations sufficiently low. Without that domain, the wall-normal velocity component belonging to vortices, which are injected into the potential flow during the breakdown of the laminar boundary layer, is interpreted as rapidly changing boundary-layer thickness, when the vortices approach the very free-stream boundary. The computation time for the interaction model is below 1% of the CPU-time of the whole numerical scheme.

3 Numerical test case

In an experiment in the laminar wind tunnel of our institute, the natural transition in a laminar separation bubble on a wing section with a chord-length of $\hat{c} = 0.615 \text{ m}$ was investigated [13]. The free-stream velocity \hat{U}_∞ is $29.3 \frac{\text{m}}{\text{s}}$. Accordingly, the chord Reynolds number is $Re_c = 1.2 \times 10^6$. In the DNS the reference length is chosen to be $\hat{L} = 0.0615 \text{ m}$. The non-dimensional streamwise location $x = 10$ is equivalent to 100% chord and the resulting Reynolds number in DNS is $Re = 1.2 \times 10^5$.

In the experiments, two velocity distributions $u_p(x)$ at the edge of the boundary layer have been measured. The first one (crosses in figure 3) refers to a flow with a separation bubble. For the turbulent second one, the separation has been suppressed by fixing a turbulator upstream of the separation bubble (circles). The difference between the two is due to displacement effects. To test the interaction model, the turbulent distribution was approximated by a polynomial function (figure 3, solid line) and prescribed as boundary-condition in the DNS. The range at the inflow boundary ($5.0 < x < 6.0$), where the velocity is constant (Blasius flow), is not shown. If the interaction model is to work properly, the DNS finally has to approximate the experimental conditions with separation bubble (crosses).

3.1 Variation of the height of the integration domain

Since the 3D part of the DNS code was unchanged, extensive 2D simulations were performed to test and validate the numerical scheme. In five simulations the height of the integration domain was varied between $y_e = 7.29 \delta_{1,s}$ (1) and $19.44 \delta_{1,s}$ (5), where $\delta_{1,s}$ denotes the displacement thickness at separation. With a constant grid spacing ($\Delta y = 0.31$) this corresponds to 145 and 385 grid points in wall-normal direction, respectively. In streamwise direction the grid has 690 points. In each case the same free-stream distribution u_p was prescribed, and a 2D TS-wave with an amplitude of $U_{TS} \equiv 10^{-4}$ was forced in the disturbance strip.

Since transition mechanisms are of our major interest, the quality of DNS results mainly depends on an accurate reproduction of the disturbance development. Thus, the independency of the DNS results from the height of the integration domain in the linear and nonlinear regime is evaluated by the comparison of the amplitude profiles of the

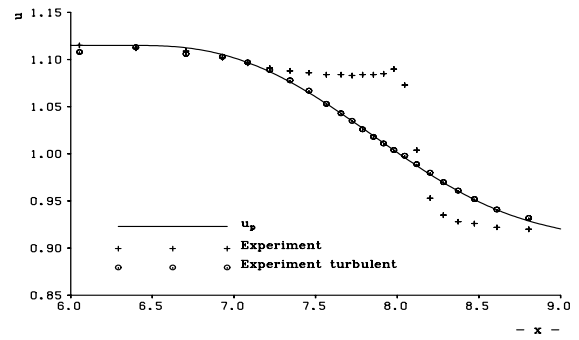


Figure 3: Edge-velocity distribution in the experiment (symbols) and boundary condition for the DNS (line). $x = 10 \equiv 100\%$ chord length.

forced TS-wave, and its first higher harmonic at three streamwise locations in the different integration domains (figure 4). The amplitudes are multiplied with a constant c_a which differs for each location. To examine the influence of displacement effects on the boundary layer, the mean profiles \bar{u} at the respective positions are also included. At the beginning of the adverse pressure gradient, location (a), the mean-flow profile has almost Blasius shape and the TS-amplitude of 0.025% is in the linear regime. Consequently, the higher harmonic is negligible (except in domain (1), solid line).

At position (b) the negative velocity of the mean flow near the wall indicates the separation bubble. The edge of the boundary layer is at $y/\delta_{1,s} \approx 3.2$ where the potential flow begins. It is significantly accelerated compared to the prescribed potential velocity at this x -position, which is included as vertical line. The deviation declines with increasing wall distance. The TS-wave is already strongly non-linear and a higher harmonic with large amplitude is present. At the upper boundary of domain (1) the TS-wave has still an amplitude of almost 1%. Nevertheless, the profile of simulation (1), solid line, fits well with the other simulations. Obviously, the interaction model derives a very accurate boundary condition for TS-waves. Behind the bubble (position c), the potential flow is decelerated. The profile has an almost turbulent shape due to the saturated TS-amplitude. The amplitude and wall-normal extend of the higher harmonic is significantly increased once more. The model predicts correct boundary conditions for disturbance waves even if disturbances with different frequencies and nonlinear amplitude are present at the free-stream boundary (in domain (1): $U_{TS}(y_e) \approx 4\%$, $U_2(y_e) \approx 1\%$). In the three highest domains (3), (4), (5) the number of sources in the interaction model was limited to

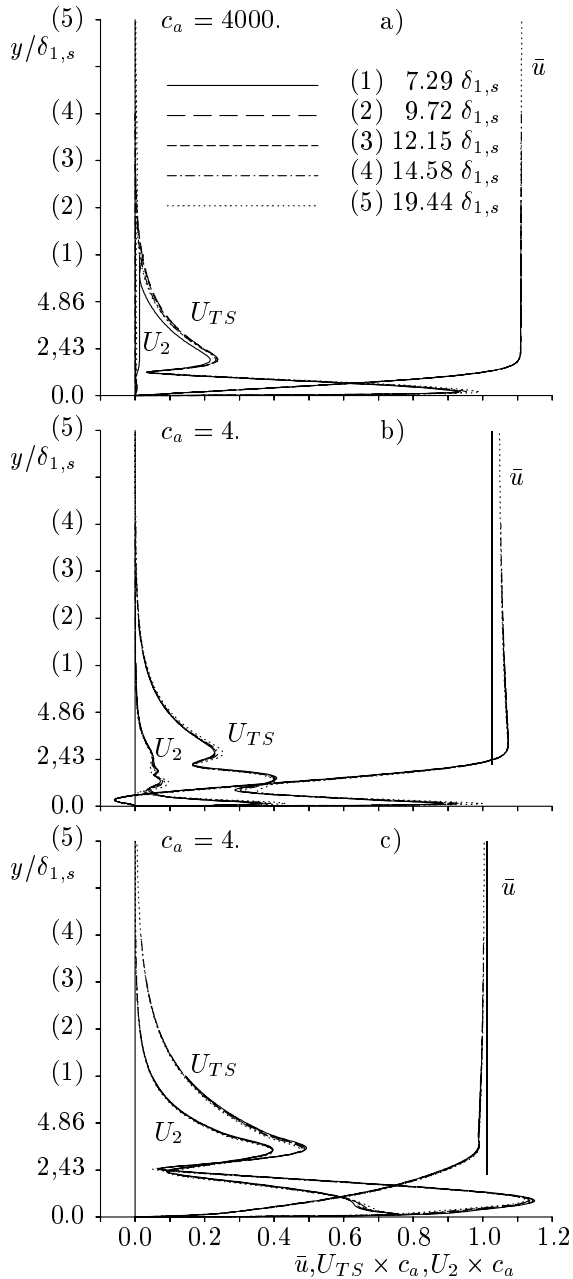


Figure 4: Comparison of the mean-flow \bar{u} , the TS-wave U_{TS} , and its first higher harmonic U_2 at a) $x = 6.5$, b) $x = 7.7$, and c) $x = 8.0$ in 5 integration domains with varying height (1) – (5). TS-wave and higher harmonic multiplied with c_a .

$I = 74$: each TS-wave length is modeled with only five sources. In the simulations (1) and (2) it is twice that number.

On the other hand, the instantaneous reaction on oscillations at the upper boundary is probably the main source of errors in the model. According to the linear stability theory (LST), the TS-wave does not cause displacement. The displacement

due to the near-wall maximum is compensated by the reverse effect of the 2nd negative maximum. The wall-normal velocity component vanishes with increasing distance from the wall and finally approaches zero. In contrast, the model takes into account only the displacement up to the location of the free-stream boundary and omits the rest. Thus, in the model, each TS-wave has a significant displacement effect. The respective sources and sinks induce oscillations at the entire free-stream boundary. The mean value of this oscillations in a TS-period is low (for a linear TS-wave it is zero). If the disturbances are periodic with respect to the TS-frequency, the mean does not vary from one TS-period to the next. In the region with polynomial function ($x < x_{ia}$) periodic flow is assumed by calculating the mean and subsequently approximating it. If the DNS finally gains the desired periodic state, this assumption introduces no additional simplifications into the numerical code but, in contrast, removes errors which are generated further downstream by the modeling of TS-waves with large amplitude and extension far to the potential flow.

To investigate the limits where the application of the model is justified, a more detailed investigation of the slight differences between the computations is necessary. Position (a) is in the region with the analytically approximated temporal behavior at the free-stream boundary ($x < x_{ia}$) and does not allow for oscillations. The fundamental profile in computation (1), solid line, differs from all other simulations, which, in contrast, fit well to each other. The difference is the largest near the free-stream boundary of integration domain (1). The fundamental wave U_{TS} has in the simulations (2) - (5) a significant amplitude at the wall-normal distance of the free-stream boundary of domain (1). In simulation (1) oscillations with fundamental frequency are suppressed, whereas a certain drift is prescribed through the polynomial function. The amplitude in simulation (1) at the free-stream boundary represents this drift and is not due to a harmonic oscillation. Thereby, the distribution in a wide range towards the wall is changed including the second maximum of the TS-wave at $y \approx 1.9 y/\delta_{1,s}$. Additionally, a higher harmonic U_2 is generated. The intended suppression of the upstream transport in the model by prescribing the analytic function, on the other hand, impairs the prediction of TS-waves. It should be noted, however, that the disturbance amplitude $U_{TS} \approx 2.5 \times 10^{-4}$ at location (a) is very small and that the near-wall maximum agrees well in all

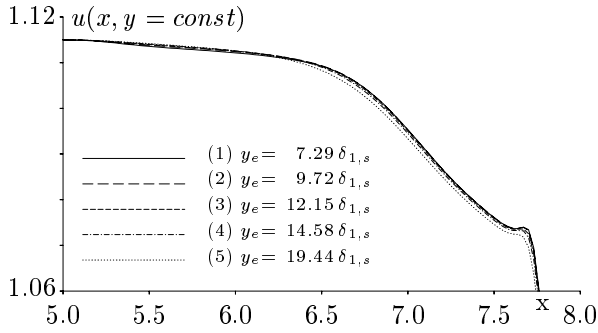


Figure 5: Comparison of the streamwise velocity component at $y = 3.24\delta_{1,s}$ in the computations (1) - (5).

computations. Moreover, the further disturbance development is not affected (positions (b) and (c)).

The disturbance amplitude in simulation (5), dotted lines, at position (a) and (b) at the near-wall maximum of the TS-wave is approximately 8% larger than in the other computations. Especially at station (b), also the whole profiles differ slightly from the other simulations. A close-up view on the velocity distribution in the potential flow at a constant distance from the wall (figure 5) shows the reason. In case (5), dotted line, the onset of the strong deceleration and the related higher TS-amplification takes place a little further upstream than in the other cases. Apart from this, the distributions are quite similar. Namely, the process of disturbance growth and disturbance saturation evolves slightly upstream in comparison with the other cases. The saturated state apparently almost freezes any further disturbance development, since the breakdown into fine-scaled turbulence is suppressed due to the lack of three-dimensionality. Therefore, when the saturated state is once attained in all computations, differences almost disappear, location (c). If three-dimensionality is considered, there would be direct impact on the onset of transition to turbulence and consequently the entire re-attachment region. Simulation (5) thus marks the upper limit, where the assumptions in the model are justified. On the contrary, domain (1) represents the lower limit since it covers just one boundary-layer thickness at the outflow boundary. In between, the results are independent of the height of the integration domain.

3.2 Variation of forcing amplitude

In the experiment neither the exact initial amplitude of the TS-waves nor their frequency distribution and spanwise wavenumber spectrum could be

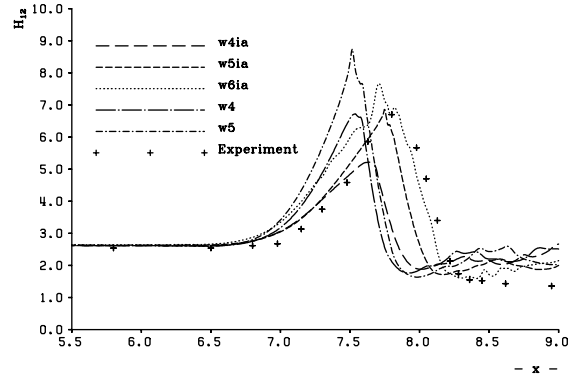


Figure 6: Comparison of the shape parameter in the experiment (symbols) and the DNS.

determined, because the TS-amplitude was far below the resolution properties of the hot-wire probe and signal-processing used. Before the interaction model was available, the separation bubble in DNS was much shorter than the one observed in the experiment. This was regarded to be due to different initial conditions of the TS-waves, especially different initial amplitudes. Therefore, 2D test calculations were made aiming at the reproduction of the experimental findings by a variation of the forced initial disturbance amplitude in DNS. However, this attempt failed. The maximum shape parameter $H_{12,max} = 6.75$ agrees well with the experiment (figure 6, symbols) if a TS-wave with an initial amplitude of $U_{TS} \equiv 10^{-4}$ is forced (case **w4**, long dash-dotted line). The location of the onset of transition and re-attachment, indicated by the decay of the shape parameter, is in case **w4** far upstream compared to the experiment. If the initial amplitude is lowered to $U_{TS} \equiv 10^{-5}$ (case **w5**, short dash-dotted line) the maximum grows strongly to $H_{12,max} = 8.75$ but still the bubble remains further upstream. This result indicates an increased height and reverse-flow intensity in the separation bubble.

3.2.1 Influence of boundary layer interaction

With the interaction model applied, in contrast, a reduction of the TS-amplitude from 10^{-4} (case **w4ia**, long dashes), to 10^{-5} (case **w5ia**, short dashes) and finally 10^{-6} (case **w6ia**, dots) delays re-attachment, and the experimental distribution in the separated region is approximated much better in cases **w5ia** and **w6ia**. Downstream of the bubble, the experimental results indicate turbulence ($H_{12} \approx 1.5$) whereas the DNS

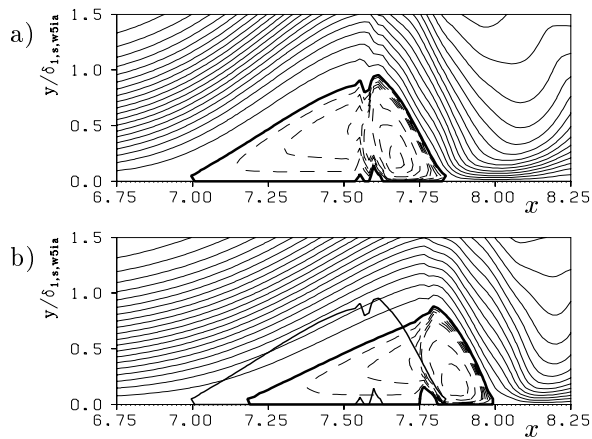


Figure 7: Isolines of time averaged streamwise velocity component with the same forcing amplitude without and with the interaction model in case **w5** a) and **w5ia** b), respectively. Lines $\bar{u} = 0$ highlighted. $\bar{u} = -0.2, -0.15, \dots, 1.0$ and $-0.04, -0.03, -0.02, -0.01$. Negative values dashed.

values are significantly higher due to the two-dimensionality. In cases with the same initial TS-amplitude the shape-parameter maximum is lower if the boundary-layer interaction is considered. This elucidates the damping influence of displacement effects on the size of the separation bubble.

The time averaged streamwise velocity fields in the vicinity of the separation bubble in the cases **w5** and **w5ia** are plotted in figure 7a) and b), respectively. The $\bar{u} = 0$ isolines are highlighted. Additionally, in figure 7b) the $\bar{u} = 0$ isoline of case **w5** is included to enable a direct comparison of size and shape of the separation bubble in both cases. The wall-normal direction is stretched by a factor of 20. As seen above, the restrictive boundary condition, which neglects interaction effects, fixes the separation bubble in streamwise direction. Thus, the flow separates further upstream and the angle of the isoline $\bar{u} = 0$ at separation is larger. The separation bubble is taller. The reverse-flow velocity maximum is 21 % U_∞ in this case and 19 % U_∞ in case **w5ia**. The shape parameter is maximum at the positions $x \approx 7.55$ (**w5**) and $x \approx 7.75$ (**w5ia**) in the two cases, which agree with those streamwise positions where the $\bar{u} > 0$ isolines have the biggest distance from the wall, but are different from the streamwise positions with the reverse-flow maximum.

The curvature of the isolines in the shear layer in the upstream part of the separation bubbles is moderate if the interaction model is applied. With-

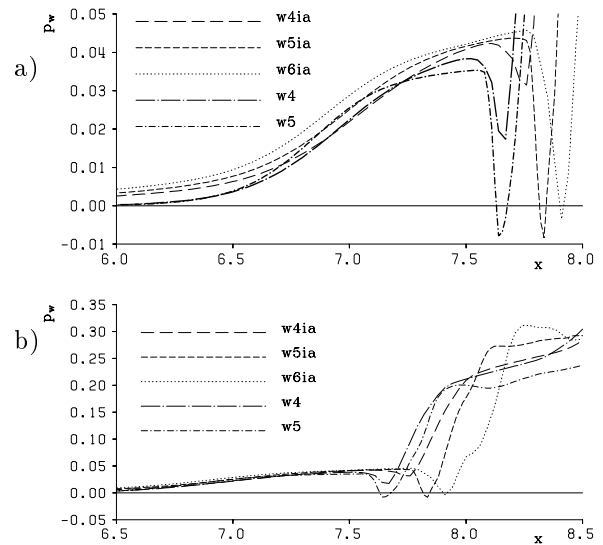


Figure 8: Wall-pressure distributions: a) in the region where separation occurs and in the front part of the bubble and b) including the re-attachment region.

out the model, the curvature is comparably strong ($x = 6.75 - 7.5$). The wall-pressure p_w helps to explain this phenomenon. The distributions show for all cases the same characteristic properties (figure 8). In the region upstream of separation and in the front part of the separation bubble ($x < 7.5$), the pressure is increasing until a strong negative peak is observed, which indicates a counter-rotating vortex in the bubble (figure 8a). Furthermore, the bubble is the tallest at approximately this location. Then, a sudden strong pressure increase occurs, indicating the diminishing height of the bubble and the strong convex curvature of the \bar{u} isolines in the re-attachment region. With interaction model, the reduction of the forcing amplitude mainly influences the location, where these characteristic properties of the pressure distribution are observed. The pressure increase in the separation region is shifted upstream in the case **w6ia**, dots in figure 8a, compared to cases **w5ia** and **w4ia**, short and long dashes, whereas the negative peak and the sudden pressure increase to growing final values is delayed (figure 8b). Without interaction model, the position of the bubble is almost fixed and the reduction of the forcing amplitude first of all causes changes of the pressure gradients. Upstream from separation ($x < 7.0$), the pressure increases much stronger in the case **w5**, short-dash dotted, than in the case **w4**, long-dash dotted in figure 8a, forcing the convex \bar{u} isolines (figure 7a). In the front part of the bubble ($7.0 < x < 7.5$), in

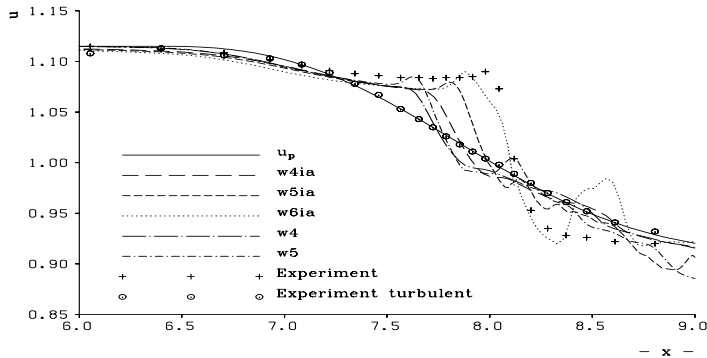


Figure 9: Comparison of the edge-velocity distribution in the experiment (symbols) and the DNS. $y/\delta_{1,s} = 4.05$ (case **w6ia** for $x > 8.12$; $y/\delta_{1,s} = 5.1$).

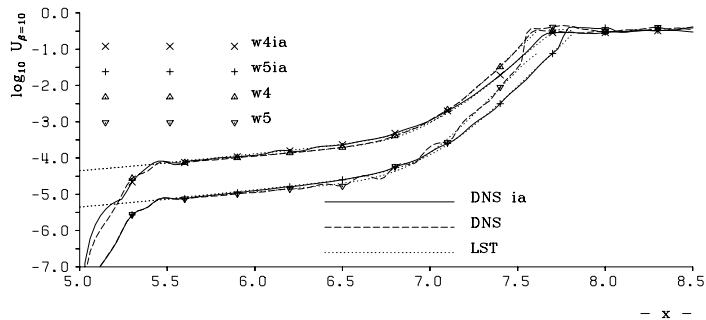


Figure 10: Amplification of the artificially excited TS-wave with the frequency $\beta = 10$: comparison of DNS (solid line with interaction model, dashed line without) with linear stability theory (dotted). $x = 10 \equiv 100\%$ chord length.

contrast, the pressure increases only weakly in case **w5** and has the lowest value of all five cases, causing concave \bar{u} isolines. The locations of the end of the sudden pressure increase in the re-attachment region and the respective final pressure levels are almost similar in the cases **w4** and **w5** (figure 8b).

The velocity distributions at the edge of the boundary layer in all simulations contain a plateau due to the displacement of the separation bubble (figure 9). Without interaction model, the lowering of the disturbance amplitude causes a strong growth of the height of the separation bubble, indicated by the high values of the shape parameter in case **w5**, that leads to an acceleration of the velocity in the pressure plateau. Taking displacement effects into account (cases **ia**) the plateau is more distinct and the distributions with different amplitude compare well with each other until in the respective simulation the deceleration below the prescribed potential distribution (solid line) begins which indicates re-attachment. The strong deceleration in the case with the lowest amplitude (**w6ia**) is at almost the same streamwise location as in the experiment. Upstream of the bubble, the edge velocity is decreased in comparison with the prescribed distribution u_p .

3.2.2 Comparison with LST

In figure 10 the amplification curves for the cases **w4**, **w4ia**, **w5**, and **w5ia** are plotted with the respective curves of the parallel linear stability the-

ory (LST, dotted lines). Initially, they depend only on the forced amplitude. The early deceleration of the potential flow in the cases with interaction model (solid line) soon causes stronger disturbance amplification and at $x \approx 6.0$ their amplitude becomes larger than in the computations without interaction model (dashed lines). At $x \approx 6.8$ an inverse behavior begins. The disturbance growth in the computations without interaction model becomes stronger and at $x \approx 7.0$ their amplitude exceeds the amplitude of the respective run using the model. Finally, the amplitude saturates at almost the same streamwise locations despite their different initial amplitudes. In contrast, with the interaction model applied, wave saturation is delayed if the initial amplitude is decreased. For all cases the agreement between DNS and the parallel linear stability theory (LST) is very good, although it could be expected that at least in the separated region the non-parallel contributions to the stability properties might be too large to justify the assumption of parallel flow.

4 Transitional LSB

So far, all comparisons between DNS and experiment were more or less of qualitative nature, since turbulence was disabled in the DNS due to the lack of 3D disturbance modes. One would expect that the latest at $x = 7.8$, where the decay of the shape parameter in the experiment indicates the

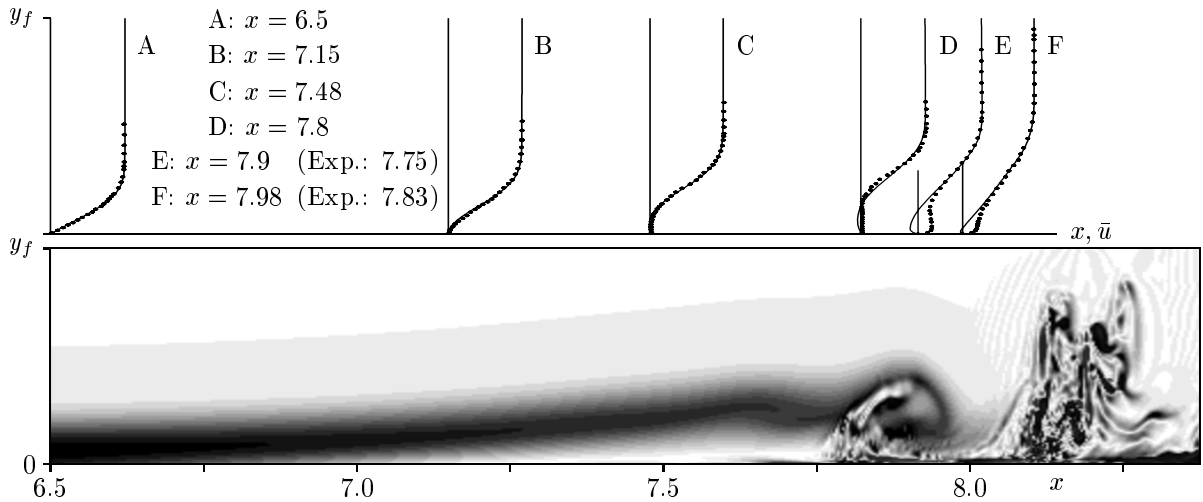


Figure 11: Top: Mean-flow profiles at different streamwise locations in the experiment (symbols) and DNS (solid lines). Bottom: Total spanwise vorticity ω_z at the centerline ($z=0$) in the vicinity of the LSB. From white to black: increasing $|\omega_z|$. $y_f = 6.08 \delta_{1,s}$.

onset of transition, 3D modes play an important role and may no longer be neglected. Thus, in another run with coarse spanwise resolution, the similarity between experiment and DNS is investigated further. Although the case **w6ia** showed the best agreement with the experimental edge-velocity distribution, it did not attain a proper periodic state which is required for the identification of small-amplitude disturbance waves under controlled conditions. Hence, a forcing amplitude of $U_{TS} \equiv 10^{-5}$ is chosen for this purpose (according to case **w5ia**). The shape-parameter maximum of case **w5ia** agrees better with the experiment than in case **w6ia**. Usually, the shape parameter is, in fact, a good measure for the size and the related stability properties of a separation bubble.

Now, a pair of weakly oblique 3D waves with the same amplitude as the 2D wave is superposed on the 2D TS-wave. Flow visualizations have shown that such waves dominate the flow upstream of the LSB in the experiment. Figure 11 shows a cut through the instantaneous spanwise vorticity in the vicinity of the LSB along the centerline of the airfoil. The mean-flow profiles (figure 11 top) are plotted at streamwise positions corresponding to the lower part of the figure. Since the separation bubble in case **w5ia** is shorter than in the experiment, the experimental profiles at locations E and F are shifted upstream by $\Delta x = -0.15$ for the comparison. This corresponds to a fitting of the decay of the experimental shape parameter to the DNS distribution of case **w5ia** in figure 6. Initially, the flow is attached (position A). The shear layer then lifts from the wall (B, C) and the pro-

files exhibit an inflection point. The flow separates at station C. Finally, a rapid disintegration of the shear layer occurs within only one TS-wavelength (D, E, F). All profiles agree well with the experiment. The differences at the positions E and F near the wall are probably due to the difficulties of the hot wire to resolve low mean velocities if the rms-amplitude is high. Moreover, at least at position E, the DNS gives evidence for the presence of reverse flow, which cannot be detected by the hot-wires either. The turbulence in DNS is not yet fully resolved and downstream of the bubble DNS results are only of qualitative nature. Therefore, better resolved DNS are required to quantitatively investigate the late non-linear stages of the transition mechanisms involved. This could help to identify the mechanisms which are possibly present in the experiment.

5 Conclusions

An improved viscous-inviscid boundary layer interaction-model has been developed, taking into account the potential equations without simplifications. Extensive 2D calculations have been performed to validate the model. Linear disturbance growth compared well with linear stability theory. Nonlinear disturbance growth was investigated by a variation of the height of the integration domain. Even when disturbances with high nonlinear amplitude are present at the free-stream boundary, the interaction model correctly predicts the instantaneous boundary values. The interaction model captures disturbance waves physically cor-

rect, even if each wave-length is resolved with less than three sources. Except for very high integration domains, the computed displacement effects of the separation bubble are independent of the height of the integration domain. The comparison of the 2D simulations with the experiment showed good qualitative agreement, although transition and turbulence were disabled in these DNS.

In comparisons of DNS with and without interaction model, it turned out that the displacement effects have a reducing influence on the size of the separation bubble. With lower forcing amplitude the length of the bubble increases and re-attachment is delayed. Without interaction model, the location of the bubble is almost fixed. The lowering of the forcing amplitude yields a taller separation bubble with stronger reverse flow and much larger shape-parameter. The flow field is characterized by strong gradients (i.e. curvature of u -isolines) in this case.

Finally, the mean profiles of a DNS with moderate spanwise resolution showed good agreement with the experiment. This and the qualitative agreement of the shape parameter and the edge velocity indicate that the improved method captures the significant physical properties of a separation bubble at high Reynolds number. Investigations of special combinations of 2D and 3D waves are, therefore, expected to be relevant for the understanding of transition in separation bubbles at Reynolds numbers typical for gliders or high-lift devices.

Acknowledgments: The authors would like to thank F. R. Hama for the proof reading and his useful comments and the Deutsche Forschungsgemeinschaft (DFG) for the financial support under contracts Ri 680/1-2 and Ri 680/1-3.

References

- [1] H. Fasel, U. Rist, and U. Konzelmann. Numerical investigation of the three-dimensional development in boundary layer transition. *AIAA J.*, 28(1): 29–37, 1990.
- [2] K. Gruber. *Numerische Untersuchungen zum Problem der Grenzschichtablösung*. Fortschritt-Berichte VDI Reihe 7. VDI-Verlag, 1988. Dissertation, Universität Stuttgart.
- [3] K. Gruber, H. Bestek, and H. Fasel. Interaction between a Tollmien-Schlichting wave and a laminar separation bubble. *AIAA* 87-1256, 1987.
- [4] M. Kloker, U. Konzelmann, and H. Fasel. Outflow boundary conditions for spatial Navier-Stokes simulations of transitional boundary layers. *AIAA J.*, 31(4): 620–628, 1993.
- [5] J. C. M. Lin and L. L. Pauley. Unsteady Laminar Separation on Low-Reynolds-Number Airfoils. *AIAA* 93-0209, 1993.
- [6] U. Maucher, U. Rist, and S. Wagner. Secondary instabilities in a laminar separation bubble. In H. Körner and R. Hilbig, editors, Volume 60 of *Notes on Numerical Fluid Mechanics*, Vieweg, 1997, 229–236.
- [7] U. Rist. Nonlinear effects of 2D and 3D disturbances on laminar separation bubbles. In S.P. Lin, editor, *Proc. "IUTAM-Symposium on Nonlinear Instability of Nonparallel flows"*. Springer, New York, 1994, 324–333.
- [8] U. Rist and H. Fasel. Direct numerical simulation of controlled transition in a flat-plate boundary layer. *J. Fluid Mech.*, 298: 211–248, 1995.
- [9] U. Rist and U. Maucher. Direct Numerical Simulation of 2-D and 3-D Instability Waves in a Laminar Separation Bubble. In *Application of Direct and Large Eddy Simulation of Transition and Turbulence*, AGARD-CP-551, 1994, 34-1–34-7.
- [10] U. Rist, U. Maucher, and S. Wagner. Direct numerical simulation of some fundamental problems related to transition in laminar separation bubbles. In Désidéri *et al.*, editors, *Computational Methods in Applied Sciences '96*, John Wiley & Sons Ltd, 1996, 319–325.
- [11] H. Schlichting and E. Truckenbrodt. *Aerodynamik des Flugzeugs*. Springer, 1st edition, 1959.
- [12] A. E. P. Veldman. New, quasi-simultaneous method to calculate interacting boundary layers. *AIAA J.*, 19(1): 79–85, 1981.
- [13] W. Würz. *Hitzdrahtmessungen zum laminar-turbulenten Strömungsumschlag in anliegenden Grenzschichten und Ablöseblasen sowie Vergleich mit der linearen Stabilitätstheorie und empirischen Umschlagskriterien*. Dissertation, Universität Stuttgart, 1995.